

Magnetic proximity effect in the two-dimensional ε-Fe_2O_3/$NbSe_2$ heterojunction

Bingyu Che(车冰玉), Guojing Hu(胡国静), Chao Zhu(朱超), Hui Guo(郭辉), Senhao Lv(吕森浩), Xuanye Liu(刘轩冶), Kang Wu(吴康), Zhen Zhao(赵振), Lulu Pan(潘禄禄), Ke Zhu(祝轲), Qi Qi(齐琦), Yechao Han(韩烨超), Xiao Lin(林晓), Zi'an Li(李子安), Chengmin Shen(申承民), Lihong Bao(鲍丽宏), Zheng Liu(刘政), Jiadong Zhou(周家东), Haitao Yang(杨海涛), and Hong-Jun Gao(高鸿钧)

Citation: Chin. Phys. B, 2024, 33 (**2**): 027502. DOI: 10.1088/1674-1056/ad09d2
Journal homepage: http://cpb.iphy.ac.cn; http://iopscience.iop.org/cpb

What follows is a list of articles you may be interested in

Stacking-dependent exchange bias in two-dimensional ferromagnetic/antiferromagnetic bilayers

Huiping Li(李慧平), Shuaiwei Pan(潘帅唯), Zhe Wang(王喆), Bin Xiang(向斌), and Wenguang Zhu(朱文光)
Chin. Phys. B, 2024, 33 (**1**): 017504. DOI: 10.1088/1674-1056/ad053d

Electric-field control of perpendicular magnetic anisotropy by resistive switching via electrochemical metallization

Yuan Yuan(袁源), Lu-Jun Wei(魏陆军), Yu Lu(卢羽), Ruo-Bai Liu(刘若柏), Tian-Yu Liu(刘天宇), Jia-Rui Chen(陈家瑞), Biao You(游彪), Wei Zhang(张维), Di Wu(吴镝), and Jun Du(杜军)
Chin. Phys. B, 2023, 32 (**6**): 067505. DOI: 10.1088/1674-1056/acbde8

In-plane current-induced magnetization reversal of Pd/CoZr/MgO magnetic multilayers

Jing Liu(刘婧), Caiyin You(游才印), Li Ma(马丽), Yun Li(李云), Ling Ma(马凌), and Na Tian(田娜)
Chin. Phys. B, 2022, 31 (**12**): 127502. DOI: 10.1088/1674-1056/ac891d

Magnetic van der Waals materials: Synthesis, structure, magnetism, and their potential applications

Zhongchong Lin(林中冲), Yuxuan Peng(彭宇轩), Baochun Wu(吴葆春), Changsheng Wang(王常生), Zhaochu Luo(罗昭初), and Jinbo Yang(杨金波)
Chin. Phys. B, 2022, 31 (**8**): 087506. DOI: 10.1088/1674-1056/ac6eed

Negative dependence of surface magnetocrystalline anisotropy energy on film thickness in $Co_{33}Fe_{67}$ alloy

De-Lai Wang(王得来), Ming-Qi Cui(崔明启), Dong-Liang Yang(杨栋亮), Jun-Cai Dong(董俊才), Wei Xu(徐伟)
Chin. Phys. B, 2016, 25 (**10**): 107501. DOI: 10.1088/1674-1056/25/10/107501

Magnetic proximity effect in the two-dimensional ε-Fe_2O_3/$NbSe_2$ heterojunction

Bingyu Che(车冰玉)[1,2,†], Guojing Hu(胡国静)[1,†], Chao Zhu(朱超)[3], Hui Guo(郭辉)[1,2], Senhao Lv(吕森浩)[1], Xuanye Liu(刘轩冶)[1,2], Kang Wu(吴康)[1,2], Zhen Zhao(赵振)[1,2], Lulu Pan(潘禄禄)[1], Ke Zhu(祝轲)[1,2], Qi Qi(齐琦)[1,2], Yechao Han(韩烨超)[1,2], Xiao Lin(林晓)[2], Zi'an Li(李子安)[4], Chengmin Shen(申承民)[1,2], Lihong Bao(鲍丽宏)[1,2], Zheng Liu(刘政)[3,¶], Jiadong Zhou(周家东)[5,§], Haitao Yang(杨海涛)[1,2,‡], and Hong-Jun Gao(高鸿钧)[1,2]

[1] *Beijing National Center for Condensed Matter Physics and Institute of Physics, Chinese Academy of Sciences, Beijing* 100190, *China*
[2] *School of Physical Sciences, University of Chinese Academy of Sciences, Beijing* 100190, *China*
[3] *School of Materials Science and Engineering, Nanyang Technological University, Singapore*
[4] *School of Physical Science and Technology, Guangxi University, Guangxi* 530004, *China*
[5] *School of Physics, Beijing Institute of Technology, Beijing* 100081, *China*

(Received 17 September 2023; revised manuscript received 28 October 2023; accepted manuscript online 6 November 2023)

Two-dimensional (2D) magnet/superconductor heterostructures can promote the design of artificial materials for exploring 2D physics and device applications by exotic proximity effects. However, plagued by the low Curie temperature and instability in air, it is hard to realize practical applications for the reported layered magnetic materials at present. In this paper, we developed a space-confined chemical vapor deposition method to synthesize ultrathin air-stable ε-Fe_2O_3 nanosheets with Curie temperature above 350 K. The ε-Fe_2O_3/$NbSe_2$ heterojunction was constructed to study the magnetic proximity effect on the superconductivity of the $NbSe_2$ multilayer. The electrical transport results show that the subtle proximity effect can modulate the interfacial spin–orbit interaction while undegrading the superconducting critical parameters. Our work paves the way to construct 2D heterojunctions with ultrathin nonlayered materials and layered van der Waals (vdW) materials for exploring new physical phenomena.

Keywords: two-dimensional heterojunctions, magnetic proximity effect, non-layered magnetic nanosheet, spin–orbit interaction

PACS: 75.70.Cn, 74.45.+c, 75.75.Cd, 75.70.Tj **DOI:** 10.1088/1674-1056/ad09d2

1. Introduction

The exchange interaction in two-dimensional (2D) magnetic heterostructures has become an intriguing research direction due to the potential of breaking the time-reversal symmetry of the originally degenerate band structures. Currently, various 2D materials have been integrated with magnetic materials, such as topological insulators,[1,2] semiconductors[3–6] and superconductors.[7] Among them, 2D magnet/superconductor heterostructures are especially interesting because both systems are closely associated with the alignment of charge spin. Intuitively, superconductivity and ferromagnetism are incompatible. However, curious phenomena arise in magnet–superconductor heterojunctions, including unconventional superconductivity, topological superconductivity, and the modulation of magnetic alignment by Ising superconductivity.[7–11] Therefore, magnet/superconductor junctions offer a great platform to study the fundamental interaction between superconductivity and magnetism. Moreover, they produce significant opportunities to develop spintronics and superconducting spintronic devices.[9]

Intrinsic 2D vdW magnets have been found in Cr, Fe, V, and Mn based materials.[12] Some of the most famous ones such as CrI_3, $Cr_2Ge_2Te_6$, and Fe_3GeTe_2 have weak ferromagnetic properties.[13–16] Without gate voltage modulation, the Curie temperatures (T_C) of these magnetic 2D vdW materials are far below room temperature, typically, 45 K for monolayer CrI_3,[13,14] 30 K for bilayer $Cr_2Ge_2Te_6$,[15] and 130 K for monolayer Fe_3GeTe_2.[16] Such low T_C results in the impossible application in the room-temperature device. Although the T_C of Fe_5GeTe_2 reaches 320 K,[17,18] magnetic 2D vdW materials reported at present are unstable in air, which hinders the exploration of their application. In contrast, nonlayered ferrimagnetic iron oxides can maintain magnetic properties up to room temperature and are stable in the ambient environment.[19] However, the study of magnetic proximity in 2D ε-Fe_2O_3-based devices is still at an embryonic stage.

In this paper, we developed a space-confined chemical vapor deposition (CVD) strategy to synthesize ultrathin ε-

[†]These authors contributed equally to this work.
[‡]Corresponding author. E-mail: htyang@iphy.ac.cn
[§]Corresponding author. E-mail: jdzhou@bit.edu.cn
[¶]Corresponding author. E-mail: z.liu@ntu.edu.sg

© 2024 Chinese Physical Society and IOP Publishing Ltd

Fe_2O_3 nanosheets with thicknesses down to 3 nm. Ultrathin ε-Fe_2O_3 nanosheets have room-temperature ferrimagnetic properties and excellent air-stability. ε-Fe_2O_3/$NbSe_2$ heterojunctions have been constructed by a standard transfer and stacking technique to explore magnetic proximity on superconductivity of $NbSe_2$ multilayers. The result shows that the subtle proximity effect of the ε-Fe_2O_3 nanosheet can modulate the spin–orbit interaction (SOI) of the $NbSe_2$ multilayer with negligible influence on its superconducting critical parameters. Our work provides a potential platform to study proximity effects in 2D heterojunctions based on ultrathin non-layered materials.

2. Experimental details

2.1. Growth of ε-Fe_2O_3 nanosheets

A space-confined CVD strategy was used to synthesize ε-Fe_2O_3 nanosheets. The ε-Fe_2O_3 nanosheets were grown on the fluorophlogopite mica (Changchun Taiyuan Fluorophlogopite Co., China) substrate. A mixture of anhydrous ferrous chloride ($FeCl_2$) and KCl powder with a mass ratio of about 10:1 was used as the precursor. A small amount of the precursor was put directly between two pieces of freshly cleaved mica (10 mm×10 mm in size). Before heating, the furnace was vacuumed and purged by pure argon to remove the residual oxygen and moisture. Then the furnace was heated to 640 °C in 15 min and held at that temperature for 2 min before cooling down naturally to room temperature, with 100 sccm Ar and 1.5 sccm O_2 flowing through the furnace during the whole process. ε-Fe_2O_3 nanosheets were grown on both pieces of mica substrates.

2.2. Sample characterization

Raman spectra were obtained by HORIBA LabRAM HR Evolution. X-ray photoelectron spectroscopy (XPS) tests were conducted in an ultrahigh vacuum system (VG ESCALAB-5) equipped with XPS. The thicknesses and the magnetic force microscopy (MFM) image of ε-Fe_2O_3 nanosheets were obtained by Oxford Cypher S atomic force microscope. The HAADF imaging was carried out on JEOL ARM-200F (S)TEM equipped with CEOS CESCOR Cs probe corrector, using a 200 kV acceleration voltage. The convergence semi-angle was set to 27–33 mrad and the collection semi-angle was 60–280 mrad for the image acquisition. Magnetization measurements were carried out by using a vibrating sample magnetometer (MPMS 3, Quantum Design). Both electrical resistance and voltage dependence of current (V–I) data were collected on a Quantum Design physical properties measurement system (PPMS).

3. Results and discussion

As shown in Fig. 1(a), ε-Fe_2O_3 has a non-symmetric orthorhombic structure, where Fe ions occupying four inequivalent sites are labeled as Fe(1), Fe(2), Fe(3), and Fe(4).[20–22] They are the centers of either an oxygen octahedron or a tetrahedron. The room-temperature ferrimagnetism of ε-Fe_2O_3 mainly comes from Fe(3) and Fe(4), whose magnetic moments are anti-collinear with different magnitudes, while the magnetic moments of Fe(1) and Fe(2) compensate for each other.[21] ε-Fe_2O_3 is a rare phase in the iron oxide family, which only exists in the nanoparticle form, not in the bulk form. It was hard to obtain pure ε-Fe_2O_3 single crystals because the synthetic routes involved phase transition.[22] However, some CVD methods have recently been introduced to synthesize air-stable ε-Fe_2O_3 nanosheets with thickness above 4 nm.[23–25] Here we developed a space-confined CVD technique to synthesize large non-layered ε-Fe_2O_3 nanosheets with thinner thicknesses than the reported ones (as described in Section 2). The thinnest thickness of our as-grown hexagonal ε-Fe_2O_3 nanosheets is down to 3 nm (Figs. 1(b) and 1(c)). The XPS spectrum across an area of 2×0.2 mm^2 confirms that all Fe ions in the nanosheets are Fe^{3+}, with no trace of Fe^{2+} (Fig. 1(d)).[26,27] As shown in Fig. 1(e), the Raman spectrum of ε-Fe_2O_3 nanosheets has four unique Raman peaks between 100 cm^{-1} and 200 cm^{-1} as hallmarks to verify the ε-Fe_2O_3 phase, which do not exist in γ-Fe_2O_3 or α-Fe_2O_3 phase.[23,28] The Raman mapping result of a typical nanosheet indicates the pure ε-Fe_2O_3 phase in the whole sample (Fig. 1(f)).

Scanning transmission electron microscopy (STEM) characterization was carried out to get a clearer understanding of the atomic arrangement and quality of the as-synthesized ε-Fe_2O_3 nanosheets. In the large-area ADF (annular dark field) image of the ε-Fe_2O_3 nanosheet along the c-axis (Fig. 2(a)), there are no lattice defects across the whole area, indicating the high crystalline quality of the nanosheet. The Fourier transform of the large-area ADF image in Fig. 2(b) shows only one set of spots, which is consistent with the simulated diffraction pattern along the c-axis of the ε-Fe_2O_3 crystal (Fig. 2(c)). In the zoomed image of the large-area ADF image, a perfect honeycomb lattice composited of spots with different brightness is observed (Fig. 2(d)). The brightness of the spots corresponds to different compositions of the atom columns beneath the sample surface. As the oxygen atoms have less contribution to the ADF signals than the iron atoms, the columns with more iron atoms are much brighter than those with fewer iron atoms. The experimental image matches well with the simulated ADF image (Fig. 2(e)) and the crystalline structure (Fig. 2(f)). The intensity of the experimental signals also agrees with the simulated data in Fig. 2(g), which demonstrates the high quality of the ε-Fe_2O_3 nanosheets.

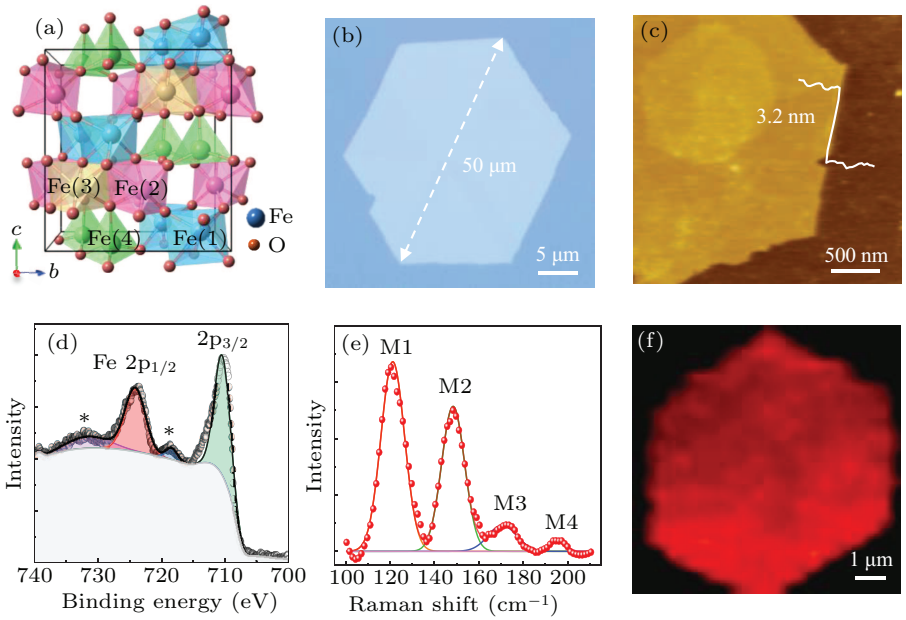


Fig. 1. (a) Crystalline structure of ε-Fe_2O_3. (b), (c) Optical and AFM images of a typical ε-Fe_2O_3 nanosheet, showing the lateral size and thickness. (d) XPS of ε-Fe_2O_3 nanosheets on the mica substrate. The circles and the lines are the experimental and fitting data. (e) Raman spectrum of the ε-Fe_2O_3 nanosheet. The red dots and the solid lines are the experimental and fitting data. (f) Raman mapping of the ε-Fe_2O_3 nanosheet, showing the uniform chemical distribution. The sum range is between 100 cm^{-1} and 200 cm^{-1}.

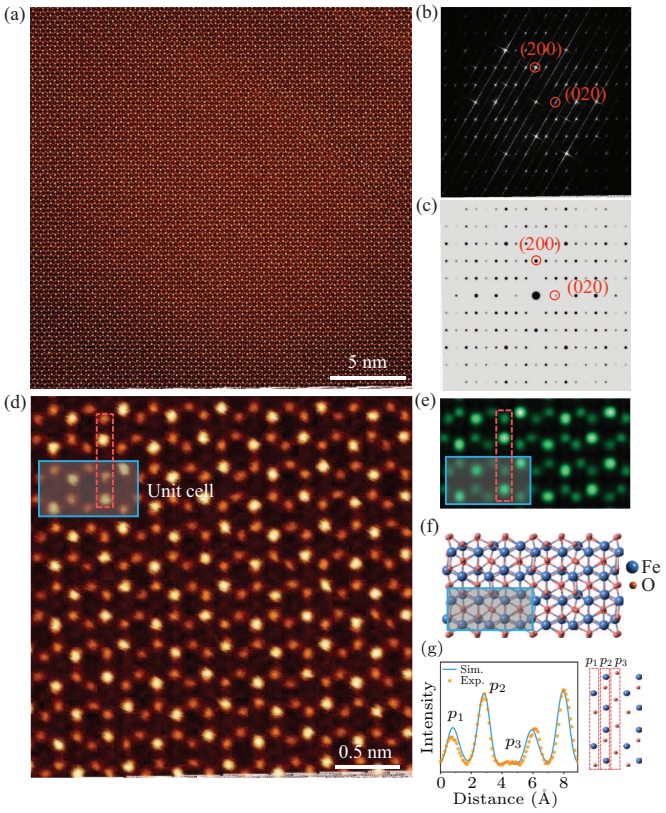


Fig. 2. STEM analysis of the ε-Fe_2O_3 nanosheet. (a) Large-area ADF-STEM image of the ε-Fe_2O_3 nanosheet. (b) The Fourier transition pattern of (a). (c) The simulated diffraction pattern of ε-Fe_2O_3. (d), (e) Zoomed ADF-STEM image of the ε-Fe_2O_3 nanosheet and its corresponding simulated image. The blue rectangular highlights one unit cell. (f) The crystalline structure along the c-axis of ε-Fe_2O_3. The highlighted unit cell in the blue rectangular perfectly matches those in (d) and (e). (g) The peak intensity of the atom columns marked by the red rectangular in (d) and (e). The yellow dots are the experimental data, which agrees well with the simulated light blue line.

To study the magnetic properties of ε-Fe_2O_3 nanosheets, temperature-dependent (M–T) and field-dependent (M–H) magnetization measurements were employed. In the M–T curves (Fig. 3(a)), the ε-Fe_2O_3 nanosheets exhibit a slight decrease of magnetization until 350 K in the field cool procedure (FC). There are also two kinks in the curve measured in the FC procedure, which is similar to that of their nanoparticle counterparts.[22,29,30] The two kinks correspond to two magnetic transitions, the one around 160 K involves the direction change of the magnetic easy axis, and the other around 133 K is related to a decrease of the coercive field. In the M–H curves under different temperatures (Fig. 3(b)), the ε-Fe_2O_3 nanosheets exhibit a well-defined hysteresis loop at 300 K, indicating ferrimagnetic properties at room temperature.[22] The magnetic force microscopy (MFM) image on a single ε-Fe_2O_3 nanosheet shows a uniform phase contrast, indicating a single domain structure at room temperature (Fig. 3(c)).

The high-quality ultrathin ε-Fe_2O_3 nanosheets with room-temperature ferrimagnetic properties can be a good candidate for exploring the magnetic proximity effect. Therefore, we constructed ε-Fe_2O_3/$NbSe_2$ heterojunctions to get further insight into magnetic proximity on superconductivity. The ultrathin ε-Fe_2O_3 nanosheet has an energy gap of about 1.9 eV, consistent with its nanoparticle counterpart.[19] Although ε-Fe_2O_3 is a non-layered material, the as-synthesized ε-Fe_2O_3 nanosheets and the mica substrate are weakly bonded.[23] Therefore, the nanosheets can be easily transferred by a standard water-assisted method. $NbSe_2$ is a van der Waals layered type-II superconductor,[31–33] which can be exfoliated into few layers to form a magnet/superconductor heterojunction with ε-Fe_2O_3 nanosheets. As the resistance of the $NbSe_2$ multilayer is much smaller than that of the ε-Fe_2O_3 nanosheet, the cur-

rent in this device can be considered to flow mainly through the $NbSe_2$ layer. To realize a precise comparison of the superconducting properties in the ε-Fe_2O_3/$NbSe_2$ heterojunction and the $NbSe_2$ multilayer, we designed a two-channel device structure on one $NbSe_2$ multilayer. As shown in Fig. 3(d), a $NbSe_2$ multilayer with uniform thickness was transferred on a group of pre-deposited parallel bottom electrodes, and then the ε-Fe_2O_3 nanosheet with a thickness of about 10 nm was stacked only on the right four electrodes to construct the ε-Fe_2O_3/$NbSe_2$ heterojunction. The electrical transport properties of the $NbSe_2$ multilayer and the ε-Fe_2O_3/$NbSe_2$ heterojunction were measured in two separate channels. The R–T curves of the $NbSe_2$ multilayer and the ε-Fe_2O_3/$NbSe_2$ heterojunction show that their critical temperatures (T_c) are 6.39 K and 6.38 K (Fig. 3(e)). The almost unchanged T_c in the heterojunction is because the in-plane magnetic moments of ε-Fe_2O_3 nanosheets generate little stray field penetrating the $NbSe_2$ multilayer.[34] The resistance dependence of out-of-plane fields (R–$H_\perp$ curves) was also measured at different temperatures. The temperature-dependent upper critical fields ($H_{c2}^{\perp}$–T) were extracted and fitted with the linear 2D Ginzburg–Landau model[35]

$$\mu_0 H_{c2}^{\perp}(T) = \frac{\Phi_0}{2\pi\xi_{GL}^2}\left(1-\frac{T}{T_c}\right),$$

where Φ_0 is the quantum flux and ξ_{GL} is the in-plane superconducting coherent length. The in-plane orbit-limiting pair breaking fields of the $NbSe_2$ multilayer and the ε-Fe_2O_3/$NbSe_2$ heterojunction are determined to be 5.68 T and 5.54 T from the extrapolation of $H_{c2}^{\perp}$ at 0 K. And the superconducting coherent lengths are calculated as 7.62 nm and 7.71 nm for the $NbSe_2$ multilayer and the heterojunction, respectively.

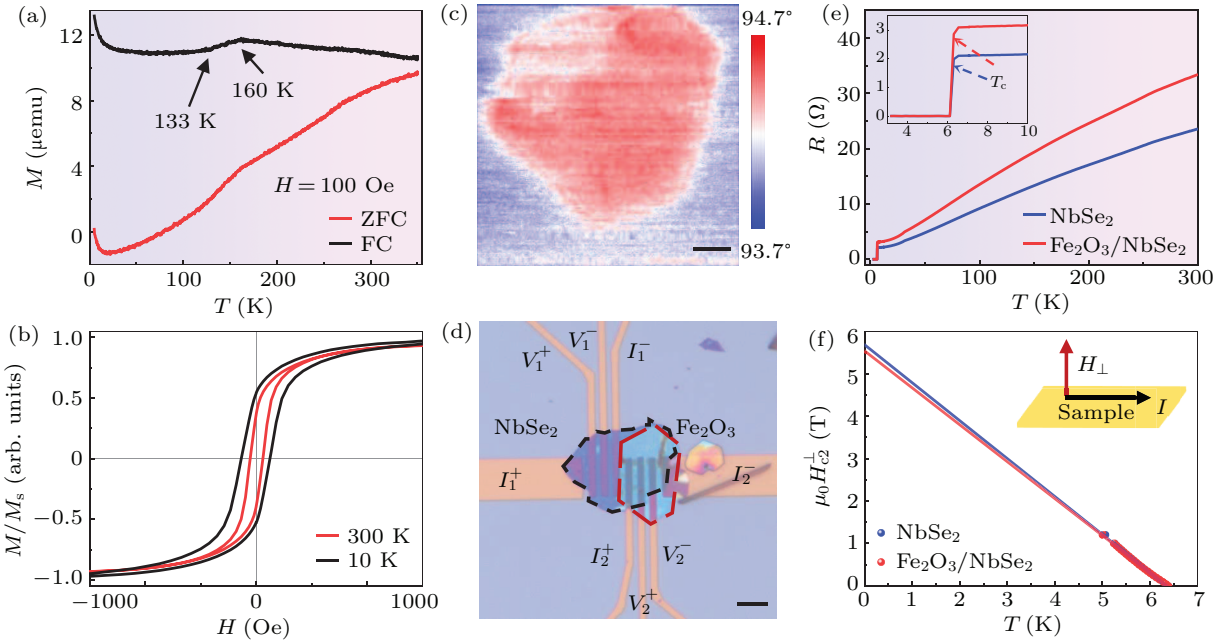


Fig. 3. Magnetic properties of ε-Fe_2O_3 nanosheets and the superconductivity of the ε-Fe_2O_3/$NbSe_2$ heterojunction. (a), (b) Temperature-dependent and field-dependent curves of ε-Fe_2O_3 nanosheets. (c) The MFM image of a typical ε-Fe_2O_3 nanosheet, indicating the uniform magnetic state. (d) The optical image of the ε-Fe_2O_3/$NbSe_2$ heterojunction device. (e) The R–T curves of the $NbSe_2$ multilayer and the ε-Fe_2O_3/$NbSe_2$ heterojunction. The inset is the R–T curves from 3 K to 10 K. T_c is defined as the temperature where the resistance reaches 90% of the normal resistance at 7 K. (f) The linear fittings for the out-of-plane upper critical magnetic fields ($H_{c2}^{\perp}$–T) of the $NbSe_2$ multilayer and the ε-Fe_2O_3/$NbSe_2$ heterojunction. H_{c2} is defined as the field where the resistance reaches 90% of the normal resistance. The scale bars in (c) and (d) are 0.5 μm and 5 μm.

The resistance dependence of the in-plane field (R–$H_\parallel$ curves) at different temperatures was also studied. Small humps are observed near the upper critical fields of the superconducting transition of the ε-Fe_2O_3/$NbSe_2$ heterojunction at high magnetic fields, while such a feature does not exist in the $NbSe_2$ multilayer (Figs. 4(a) and 4(b)). The humps are probably induced by the flow of Josephson vortices. The applied in-plane fields will induce interlayer Josephson vortices in the $NbSe_2$ multilayer, which penetrate the ε-Fe_2O_3 nanosheet. Since the vortices are weakly pinned in the ε-Fe_2O_3 nanosheet, when a current perpendicular to the field flows through them, the vortices can be de-pinned and driven by the Lorentz force. The collective movement of the Josephson vortices leads to large energy dissipation and results in a limited magnetoresistance.[36,37] The $H_{c2}^{\parallel}$–T curves were also plotted and fitted with in-plane 2D Ginzburg–Landau model[35]

$$\mu_0 H_{c2}^{\parallel}(T) = \frac{\Phi_0\sqrt{12}}{2\pi\xi_{GL}d_{SC}}\sqrt{1-\frac{T}{T_c}},$$

where d_{SC} is the effective thickness of the superconductor.

The superconducting effective thicknesses can be obtained to be 8.53 nm and 8.94 nm for the $NbSe_2$ multilayer and the ε-Fe_2O_3/$NbSe_2$ heterojunction. Thus, the obtained T_c, H_{c2}, ξ_{GL} and d_{SC} in the $NbSe_2$ multilayer and ε-Fe_2O_3/$NbSe_2$ heterojunction are concluded nearly the same.

Besides T_c and H_{c2}, the critical supercurrent (I_c) is another important parameter for a superconductor. Therefore, V–I curves for both the $NbSe_2$ multilayer and the ε-Fe_2O_3/$NbSe_2$ heterojunction were also measured to study the magnetic proximity effect on superconducting properties. Although the I_c is nearly the same at about 0.45 mA for both the $NbSe_2$ multilayer and the ε-Fe_2O_3/$NbSe_2$ heterojunction, the transition from the superconducting state to normal state (ΔI) is different (Fig. 4(d)). The ΔI for the heterojunction is much larger than that for the $NbSe_2$ multilayer, which might result from the interaction between the magnetic moment of the ε-Fe_2O_3 nanosheet and the magnetic flux generated by the current in the $NbSe_2$ multilayer.[38] The V–I measurements were also carried out under different out-of-plane magnetic fields. The field-dependent critical currents I_c^+ (I_c^-) at a positive (negative) bias were extracted from the V–I curves. A field-induced nonreciprocal charge transport for the $NbSe_2$ multilayer was observed (Fig. 4(e)), which is significantly suppressed in the ε-Fe_2O_3/$NbSe_2$ heterojunction (Fig. 4(f)). The nonreciprocal critical current under positive and negative bias originates from the valley-Zeeman spin–orbit interaction (SOI) of $NbSe_2$.[39,40] In $NbSe_2$ few layers, the electron spin is locked with valleys in the out-of-plane direction.[41] When an out-of-plane field is applied, the degeneracy of valleys with opposite momenta is broken by the Zeeman effect, which will possibly induce asymmetric pinning potentials in the $NbSe_2$ multilayer.[42] And the collective flow of the vortices in the $NbSe_2$ multilayer driven by the external charge current among these asymmetric pinning potentials will cause nonreciprocal transport behavior.[40,43] This phenomenon is suppressed under high fields, similar to the previously reported results.[40,44–47] In the heterojunction, the ε-Fe_2O_3 nanosheet on top of the $NbSe_2$ multilayer might generate a complex pinning effect that competes with the asymmetric pinning potentials generated by the valley-Zeeman SOI in $NbSe_2$ to interference the vortex flow, and therefore suppresses the nonreciprocal transport behavior. The results indicate that the strong SOI exists at the interface between the nonlayered ε-Fe_2O_3 nanosheet and the $NbSe_2$ multilayer, and prove that the ε-Fe_2O_3 nanosheets are smooth and clean enough to construct 2D heterojunctions.

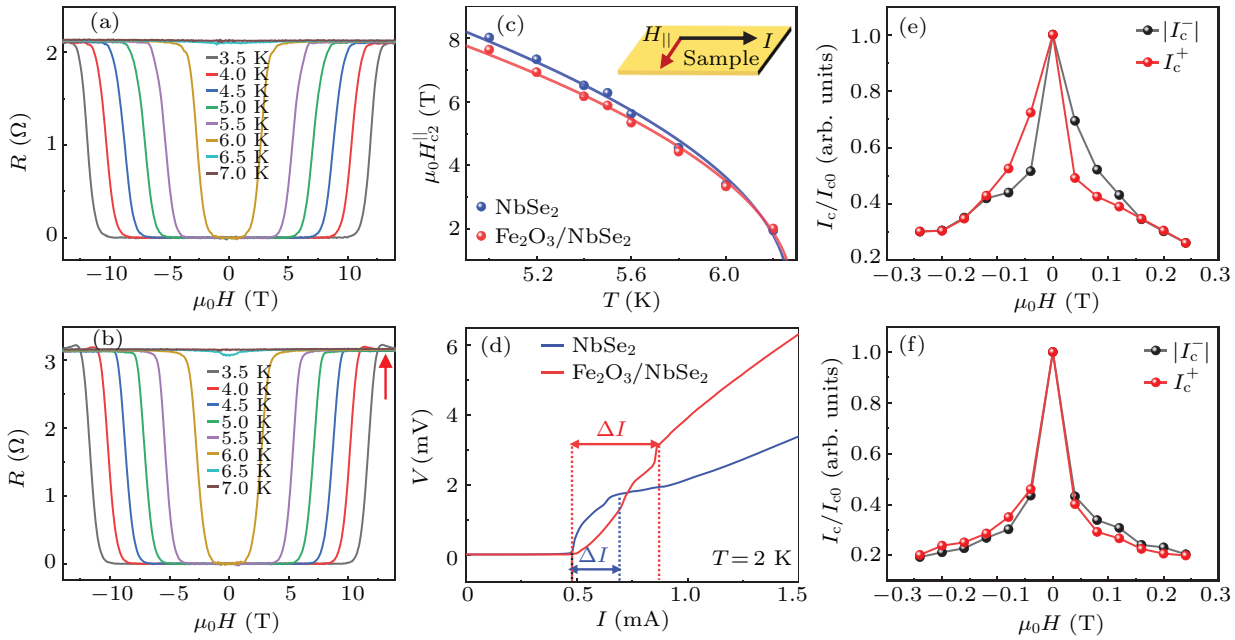


Fig. 4. Electrical transport properties of the $NbSe_2$ multilayer and the ε-Fe_2O_3/$NbSe_2$ heterojunction. (a), (b) The R–H curves of the $NbSe_2$ and the ε-Fe_2O_3/$NbSe_2$ heterojunction regions. The red arrow in (b) indicates the hump which appears near $H_{c2}^{\parallel}$ at high fields. (c) The fitting curves for in-plane $H_{c2}^{\parallel}$–T of the $NbSe_2$ multilayer and the ε-Fe_2O_3/$NbSe_2$ heterojunction. (d) The V–I curves of the $NbSe_2$ multilayer and the ε-Fe_2O_3/$NbSe_2$ heterojunction at 2 K. ΔI is the current range of superconducting transition. (e), (f) The out-of-plane magnetic field-dependent positive and negative I_c extracted from the V–I curves of the $NbSe_2$ multilayer and the ε-Fe_2O_3/$NbSe_2$ heterojunction.

4. Conclusion

We successfully synthesized high-quality ε-Fe_2O_3 nanosheets by a space-confined CVD method and verified its high crystalline quality by STEM characterization. The magnetic measurements show that the ε-Fe_2O_3 nanosheets remain ferrimagnetic up to 350 K. An ultrathin ε-Fe_2O_3 nanosheet was used to construct the ε-Fe_2O_3/$NbSe_2$ heterojunction to study the magnetic proximity effect on superconductivity of $NbSe_2$ multilayer. The electrical transport results demonstrate that the T_c, H_{c2} and I_c in the $NbSe_2$ multilayer and

ε-Fe_2O_3/$NbSe_2$ heterojunction are nearly the same, indicating that the ε-Fe_2O_3 nanosheet has a minor influence on the superconductivity of the $NbSe_2$ multilayer. However, the proximity effect of the ε-Fe_2O_3 nanosheet shows an obvious modulation effect on the interfacial SOI, which suppresses the nonreciprocal transport of the $NbSe_2$ multilayer. This work shows that non-layered ferrimagnetic ε-Fe_2O_3 nanosheets can form 2D heterojunctions with other 2D vdW materials to modulate their properties by proximity effect, which enables the ε-Fe_2O_3 nanosheets and further non-layered 2D magnets with stronger perpendicular anisotropy[48] to be potential building blocks for spintronics and superconducting spintronic devices.

Acknowledgements

We thank Gangqin Liu for the helpful discussions. The work is supported by the National Key Research and Development Program of China (Grant No. 2022YFA1204104), the National Natural Science Foundation of China (Grant No. 61888102), the Chinese Academy of Sciences (Grant Nos. ZDBS-SSW-WHC001 and XDB33030100).

References

[1] Lee C, Katmis F, Jarillo-Herrero P, Moodera J S and Gedik N 2016 *Nat. Commun.* **7** 12014
[2] Katmis F, Lauter V, Nogueira F S, Assaf B A, Jamer M E, Wei P, Satpati B, Freeland J W, Eremin I, Heiman D, Jarillo-Herrero P and Moodera J S 2016 *Nature* **533** 513
[3] MacDonald A H, Schiffer P and Samarth N 2005 *Nat. Mater.* **4** 195
[4] Zhong D, Seyler K L, Linpeng X, Cheng R, Sivadas N, Huang B, Schmidgall E, Taniguchi T, Watanabe K, McGuire M A, Yao W, Xiao D, Fu K C and Xu X 2017 *Sci. Adv.* **3** e1603113
[5] Seyler K L, Zhong D, Huang B, Linpeng X, Wilson N P, Taniguchi T, Watanabe K, Yao W, Xiao D, McGuire M A, Fu K M and Xu X 2018 *Nano Lett.* **18** 3823
[6] Zhao C, Norden T, Zhang P, Zhao P, Cheng Y, Sun F, Parry J P, Taheri P, Wang J, Yang Y, Scrace T, Kang K, Yang S, Miao G X, Sabirianov R, Kioseoglou G, Huang W, Petrou A and Zeng H 2017 *Nat. Nanotechnol.* **12** 757
[7] Buzdin A I 2005 *Rev. Mod. Phys.* **77** 935
[8] Bergeret F S, Volkov A F and Efetov K B 2005 *Rev. Mod. Phys.* **77** 1321
[9] Eschrig M 2015 *Reports on Progress in Physics* **78** 104501
[10] Beenakker C W J 2013 *Annual Review of Condensed Matter Physics* **4** 113
[11] Aikebaier F, Heikkilä T T and Lado J L 2022 *Phys. Rev. B* **105** 054506
[12] Yao Y, Zhan X, Sendeku M G, Yu P, Dajan F T, Zhu C, Li N, Wang J, Wang F, Wang Z and He J 2021 *Nanotechnology* **32** 472001
[13] McGuire M A, Dixit H, Cooper V R and Sales B C 2015 *Chemistry of Materials* **27** 612
[14] Dillon J F and Olson C E 1965 *J. Appl. Phys.* **36** 1259
[15] Gong C, Li L, Li Z, Ji H, Stern A, Xia Y, Cao T, Bao W, Wang C, Wang Y, Qiu Z Q, Cava R J, Louie S G, Xia J and Zhang X 2017 *Nature* **546** 265
[16] Deng Y, Yu Y, Song Y, Zhang J, Wang N Z, Sun Z, Yi Y, Wu Y Z, Wu S, Zhu J, Wang J, Chen X H and Zhang Y 2018 *Nature* **563** 94
[17] Zhao B, Ngaloy R, Ghosh S, Ershadrad S, Gupta R, Ali K, Hoque A M, Karpiak B, Khokhriakov D, Polley C, Thiagarajan B, Kalaboukhov A, Svedlindh P, Sanyal B and Dash S P 2023 *Adv. Mater.* **35** 2209113
[18] May A F, Ovchinnikov D, Zheng Q, Hermann R, Calder S, Huang B, Fei Z, Liu Y, Xu X and McGuire M A 2019 *ACS Nano* **13** 4436
[19] Cornell R M and Schwertmann U 2003 *The iron oxides: structure, properties, reactions, occurrences, and uses* (Weinheim: Wiley-vch) pp. 111–137
[20] Kelm K and Mader W 2005 *Z. Anorg. Allg. Chem.* **631** 2383
[21] Gich M, Frontera C, Roig A, Taboada E, Molins E, Rechenberg H R, Ardisson J D, Macedo W A A, Ritter C, Hardy V, Sort J, Skumryev V and Nogués J 2006 *Chemistry of Materials* **18** 3889
[22] Tuček J, Zbořil R, Namai A and Ohkoshi S I 2010 *Chemistry of Materials* **22** 6483
[23] Yuan J, Balk A, Guo H, Fang Q, Patel S, Zhao X, Terlier T, Natelson D, Crooker S and Lou J 2019 *Nano Lett.* **19** 3777
[24] Wang Y, Wang P, Wang H, Xu B, Li H, Cheng M, Feng W, Du R, Song L, Wen X, Li X, Yang J, Cai Y, He J, Wang Z and Shi J 2023 *Adv. Mater.* **35** 2209465
[25] Zhao Z, Fang Z, Han X, Yang S, Zhou C, Zeng Y, Zhang B, Li W, Wang Z, Zhang Y, Zhou J, Zhou J, Ye Y, Hou X, Zhao X, Gao S and Hou Y 2023 *Nat. Commun.* **14** 958
[26] Liu S, Wang S, Guo J and Guo Q 2012 *RSC Advances* **2** 9938
[27] Xue M, Wang S, Wu K, Guo J and Guo Q 2011 *Langmuir* **27** 11
[28] López-Sánchez J, Serrano A, Del Campo A, Abuín M, Rodríguez de la Fuente O and Carmona N 2016 *Chemistry of Materials* **28** 511
[29] Gich M, Roig A, Frontera C, Molins E, Sort J, Popovici M, Chouteau G, Martín y Marero D and Nogués J 2005 *J. Appl. Phys.* **98** 044307
[30] Sakurai S, Jin J, Hashimoto K and Ohkoshi S I 2005 *J. Phys. Soc. Jpn.* **74** 1946
[31] Frindt R F 1972 *Phys. Rev. Lett.* **28** 299
[32] Dvir T, Massee F, Attias L, Khodas M, Aprili M, Quay C H L and Steinberg H 2018 *Nat. Commun.* **9** 598
[33] Ugeda M M, Bradley A J, Zhang Y, Onishi S, Chen Y, Ruan W, Ojeda-Aristizabal C, Ryu H, Edmonds M T, Tsai H-Z, Riss A, Mo S K, Lee D, Zettl A, Hussain Z, Shen Z X and Crommie M F 2016 *Nat. Phys.* **12** 92
[34] Ahamed I, Pathak R, Skomski R and Kashyap A 2018 *AIP Advances* **8** 055815
[35] Tinkham M and Emery V 1996 *Physics Today* **49** 74
[36] Uji S, Terashima T, Nishimura M, Takahide Y, Konoike T, Enomoto K, Cui H, Kobayashi H, Kobayashi A, Tanaka H, Tokumoto M, Choi E S, Tokumoto T, Graf D and Brooks J S 2006 *Phys. Rev. Lett.* **97** 157001
[37] Jiang D, Yuan T, Wu Y, Wei X, Mu G, An Z and Li W 2020 *ACS Applied Materials & Interfaces* **12** 49252
[38] Khanukov A, Mangel I, Wissberg S, Keren A and Kalisky B 2022 *Phys. Rev. B* **106** 144510
[39] He J J, Tanaka Y and Nagaosa N 2022 *New J. Phys.* **24** 053014
[40] Bauriedl L, Bäuml C, Fuchs L, Baumgartner C, Paulik N, Bauer J M, Lin K Q, Lupton J M, Taniguchi T, Watanabe K, Strunk C and Paradiso N 2022 *Nat. Commun.* **13** 4266
[41] Xi X, Wang Z, Zhao W, Park J H, Law K T, Berger H, Forró L, Shan J and Mak K F 2016 *Nat. Phys.* **12** 139
[42] Zhang E, Xu X, Zou Y C, Ai L, Dong X, Huang C, Leng P, Liu S, Zhang Y, Jia Z, Peng X, Zhao M, Yang Y, Li Z, Guo H, Haigh S J, Nagaosa N, Shen J and Xiu F 2020 *Nat. Commun.* **11** 5634
[43] Hoshino S, Wakatsuki R, Hamamoto K and Nagaosa N 2018 *Phys. Rev. B* **98** 054510
[44] Ando F, Miyasaka Y, Li T, Ishizuka J, Arakawa T, Shiota Y, Moriyama T, Yanase Y and Ono T 2020 *Nature* **584** 373
[45] Baumgartner C, Fuchs L, Costa A, Reinhardt S, Gronin S, Gardner G C, Lindemann T, Manfra M J, Faria Junior P E, Kochan D, Fabian J, Paradiso N and Strunk C 2022 *Nat. Nanotechnol.* **17** 39
[46] Yuan N F Q and Fu L 2022 *Proc. Natl. Acad. Sci. USA* **119** e2119548119
[47] Ilić S and Bergeret F 2022 *Phys. Rev. Lett.* **128** 177001
[48] Bian M, Zhu L, Wang X, Choi J, Chopdekar R V, Wei S, Wu L, Huai C, Marga A, Yang Q, Li Y C, Yao F, Yu T, Crooker S A, Cheng X M, Sabirianov R F, Zhang S, Lin J, Hou Y and Zeng H 2022 *Adv. Mater.* **34** 2200117